

Graphene-based Josephson junction microwave bolometer

<https://doi.org/10.1038/s41586-020-2752-4>

Received: 3 April 2019

Accepted: 8 July 2020

Published online: 30 September 2020

 Check for updates

Gil-Ho Lee^{1,2}, Dmitri K. Efetov³, Woonchan Jung², Leonardo Ranzani⁴, Evan D. Walsh^{5,6}, Thomas A. Ohki⁴, Takashi Taniguchi⁷, Kenji Watanabe⁸, Philip Kim¹, Dirk Englund⁶ & Kin Chung Fong⁴✉

Sensitive microwave detectors are essential in radioastronomy¹, dark-matter axion searches² and superconducting quantum information science^{3,4}. The conventional strategy to obtain higher-sensitivity bolometry is the nanofabrication of ever smaller devices to augment the thermal response^{5–7}. However, it is difficult to obtain efficient photon coupling and to maintain the material properties in a device with a large surface-to-volume ratio owing to surface contamination. Here we present an ultimately thin bolometric sensor based on monolayer graphene. To utilize the minute electronic specific heat and thermal conductivity of graphene, we develop a superconductor–graphene–superconductor Josephson junction^{8–13} bolometer embedded in a microwave resonator with a resonance frequency of 7.9 gigahertz and over 99 per cent coupling efficiency. The dependence of the Josephson switching current on the operating temperature, charge density, input power and frequency shows a noise-equivalent power of 7×10^{-19} watts per square-root hertz, which corresponds to an energy resolution of a single 32-gigahertz photon¹⁴, reaching the fundamental limit imposed by intrinsic thermal fluctuations at 0.19 kelvin. Our results establish that two-dimensional materials could enable the development of bolometers with the highest sensitivity allowed by the laws of thermodynamics.

Many attractive electrical and thermal properties make graphene a promising material for bolometry and calorimetry^{15–22}. Graphene can absorb photons from a wide frequency bandwidth efficiently by impedance matching²³; the electron–electron scattering time is short and can quickly equilibrate the internal energy from absorbed photons to prevent leakage through optical phonon emission²⁴; its weak electron–phonon coupling can keep the electrons thermally isolated from the lattice^{10,15,16,25–29}; and, most importantly, at the charge-neutrality point, it has a vanishing density of states. This results in a small heat capacity and electron-to-phonon thermal conductance, which are highly desirable material properties for bolometers and calorimeters, while maintaining a short thermal response time¹⁹. Although the bolometric response of graphene has been tested in devices based on noise thermometry^{16,18,19}, their performance is severely hampered by degradation in the thermometer sensitivity when the electron temperature rises upon photon absorption¹⁸. Here, we overcome this challenge by adopting a fundamentally different measurement technique: we integrate monolayer graphene simultaneously into a microwave resonator and a Josephson junction; upon the absorption of microwave radiation into the resonator, the rise of the electron temperature in graphene suppresses the switching current of the superconductor–graphene–superconductor (SGS) Josephson junction. This mechanism can function as the bolometer readout and enable us to study the thermal response of this bolometer.

Inspired by the use of heating or quasiparticle injection to control the supercurrent in superconductor–normal–superconductor junctions in the d.c. regime^{30,31}, we design our microwave bolometer with a orthogonal-terminal graphene-based Josephson junction (GJJ) as shown in Fig. 1a, b. The monolayer graphene is encapsulated by hexagonal boron nitride (hBN) at the top and bottom. The proximitized Josephson junction (green colour) is formed by edge-contacting NbN superconductors to the graphene so that dissipationless Josephson current can flow along the direction of the Josephson junction¹¹. A dissipative microwave current can flow along the direction perpendicular to that of the junction, and the graphene extends out from each side of the GJJ by 0.8 μm before connecting to quarter-wave resonators (blue colour) to form a half-wave resonator using a NbN microstrip with a characteristic impedance of 86 Ω (Fig. 1c, d). This extension is narrow and long to prevent Josephson coupling to the microstrips, and positions the graphene at the current antinode of the resonator. We measured three devices with intended variations in graphene dimensions, superconductors and input frequencies to test the performance of the bolometer. Whereas their results are similar, here we present the device with the highest sensitivity and the other two are presented in Extended Data Table 1 and Extended Data Figs. 2–4.

Microwave power is applied to the resonator through a 200-fF coupling capacitor. We can characterize our GJJ-embedded resonator by

¹Department of Physics, Harvard University, Cambridge, MA, USA. ²Department of Physics, Pohang University of Science and Technology, Pohang, Republic of Korea. ³ICFO-Institut de Ciències Fotòniques, The Barcelona Institute of Science and Technology, Barcelona, Spain. ⁴Quantum Engineering and Computing Group, Raytheon BBN Technologies, Cambridge, MA, USA. ⁵Department of Electrical Engineering and Computer Science, Massachusetts Institute of Technology, Cambridge, MA, USA. ⁶School of Engineering and Applied Sciences, Harvard University, Cambridge, MA, USA. ⁷International Center for Materials Nanoarchitectonics, National Institute for Materials Science, Tsukuba, Japan. ⁸Research Center for Functional Materials, National Institute for Materials Science, Tsukuba, Japan. ✉e-mail: kc.fong@raytheon.com

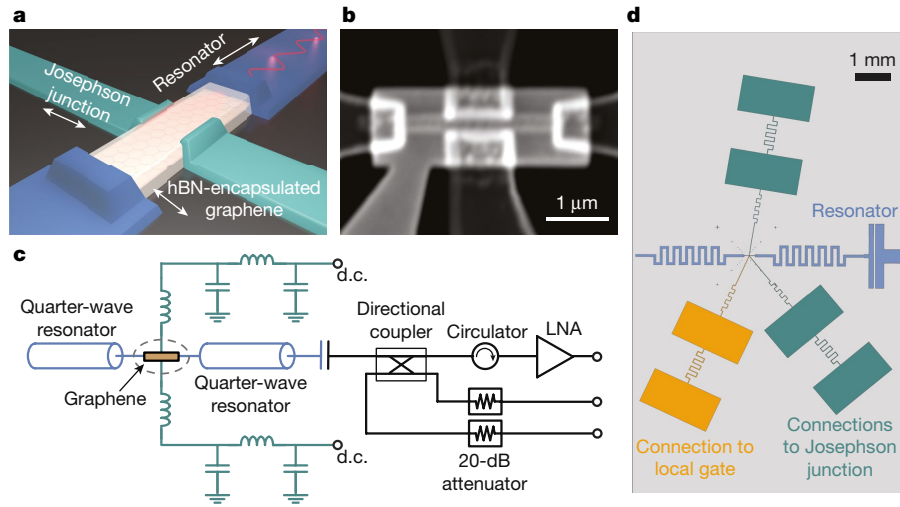


Fig. 1 | Graphene-based Josephson junction microwave bolometer. **a**, Device concept of the SGS Josephson junction microwave bolometer. The hBN-encapsulated SGS Josephson junction (1 μm wide, with a gap of $\sim 0.3 \mu\text{m}$) is embedded simultaneously in a half-wave resonator to allow microwave coupling (blue) and the d.c. readout (green) of the Josephson junction. For clarity, the local gate is not shown. **b**, Scanning electron microscope image of the orthogonal-terminal Josephson junction. **c**, Schematic of the detector

setup. The graphene flake is located at the current antinode of the half-wave microwave resonator. The test microwave power is coupled to the detector through the 20-dB directional coupler, attenuators and coaxial cables. Reflected power is measured by a low-noise amplifier. Two stages of inductors and capacitors form a low-pass filter network for the d.c. measurement. **d**, False-colour optical image of the actual device.

reflectometry using a directional coupler. The test power is delivered via microwave coaxial cables with attenuators to filter the thermal noise at room temperature. To decouple the GJJ d.c. measurement from the microwave resonator, two stages of LC low-pass filters are implemented to form a high-impedance line at high frequency. The 1-nH inductors are made of narrow meandered wires and are shunted by 530-fF capacitor plates.

We study GJJ switching as a function of temperature and gate voltage. Figure 2a shows the typical voltage drop across the junction, V_{JJ} , as the d.c. bias current is swept from 1.5 μA to $-1.5 \mu\text{A}$ at device temperatures between 0.19 K and 0.9 K. Our GJJ shows hysteretic switching behaviour: the switching current I_s at which the junction switches from the dissipationless state to the normal state is different from the retrapping current, I_r . Such hysteresis is presumably due to Joule self-heating when the junction turns normal¹⁰. The average switching currents $\langle I_s \rangle$ are plotted at various gate voltages V_g and temperatures T in Fig. 2b, c. The drop of $\langle I_s \rangle$ with increasing temperature is an important feature that can determine the sensitivity of the GJJ as a bolometer, as well as the quantum efficiency and dark count of a future microwave single-photon detector²³. Figure 2d shows a plot of the normal-state junction resistance R_n as a function of gate voltage, which indicates that the charge-neutrality point is at -0.9 V . We note that the unusual rise of R_n at $V_g \approx 2\text{--}3 \text{ V}$ may be due to the formation of a moiré superlattice with the hBN substrate (see Methods). The product $\langle I_s \rangle R_n$ is of the order of 0.16 mV, which is comparable to that of other GJJs of similar size in the long diffusive limit²³.

The coupling efficiency can be characterized using reflectometry (see Fig. 3a). We designed the resonator to be critically coupled at about 7.9 GHz. The dissipation is dominated by the monolayer graphene, which can be modelled as a resistor located at the current antinode. At an input power of -112 dBm , we measured the change in $\langle I_s \rangle$ as a function of input frequency for two different gate voltages, 0.1 V and 1.3 V, with $\langle I_s \rangle$ of 0.94 μA and 1.17 μA , respectively (see Fig. 3b). If the absorbed microwave photon caused a resonant excitation at the plasma frequency of the GJJ, we would expect the frequency of the resonance dip in $\langle I_s \rangle$ to shift by approximately 1 GHz, because the GJJ plasma frequency is proportional to the square root of the critical current. By contrast, the suppression of $\langle I_s \rangle$ aligns closely to the microwave resonance

frequency measured by reflectometry. Therefore, we cannot attribute the suppression of $\langle I_s \rangle$ to resonant excitation of the GJJ. We note that the linewidths in Fig. 3b match to those given by the loaded quality factors of 9 and 13 at $V_g = 0.1 \text{ V}$ and 1.3 V , respectively, obtained from the fitting of the phase of the scattering parameter in Fig. 3a.

Supercurrent switching statistics can reveal the basic properties of the GJJ^{8,9} and hence its thermal response as a bolometer. We measure the distribution of I_s by recording the potential drop across the GJJ while sweeping the bias current 6,000 times for each gate voltage, input power and temperature. The switching of the GJJ from the supercurrent state to the normal state is stochastic, and the typical distribution is plotted in Fig. 4a at 0.19 K and 0.45 K and at $V_g = 0.1 \text{ V}$ without power input. The switching rate (also known as the escape rate from the tilted-washboard potential in the resistively and capacitively shunted junction model), and thus the switching probability, can be determined uniquely from the distribution using the Fulton–Dunkleberger method^{8,9}. When the experiment is conducted at 0.19 K with an increasing power input, the switching histogram shifts gradually to lower values. When the microwave input power reaches 126 fW, when the device is at 0.19 K, the distribution overlaps well with that at 0.45 K with zero input power; therefore, the GJJ has the same switching rate under these two conditions. This suggests that the suppression of $\langle I_s \rangle$ is due to the heating of graphene electrons from 0.19 K to 0.45 K by the microwave input power, and not of other mechanisms such as the a.c. Josephson effect or an additional bias current across the GJJ³².

$\langle I_s \rangle$ decreases monotonically as we raise the microwave input power P_{mw} . Figure 4b shows $\langle I_s \rangle$ as a function of input power. Using the measured $\langle I_s \rangle$ at various device temperatures in Fig. 2b, we can apply an interpolation to calculate the graphene electron temperature T_e as a function of $\langle I_s \rangle$, which is a function of P_{mw} . The results, $T_e(P_{\text{mw}})$, are shown in Fig. 4c for four different gate voltages, with offsets of multiples of 0.19 K in the y axis for clarity. The dashed lines denote fits to the data using the electron–phonon heat transfer equation^{25–27} $P = \Sigma A(T_e^\delta - T^\delta)$, where A is the area of the monolayer graphene, and Σ and δ are the electron–phonon coupling parameter and its temperature power-law exponent, respectively. The best-fit Σ values are 2.14, 2.04, 2.74 and 3.30 $\text{W m}^{-2} \text{K}^{-3}$ in ascending order of gate voltages with $\delta = 3$. This temperature power law corresponds to the cooling of graphene electrons

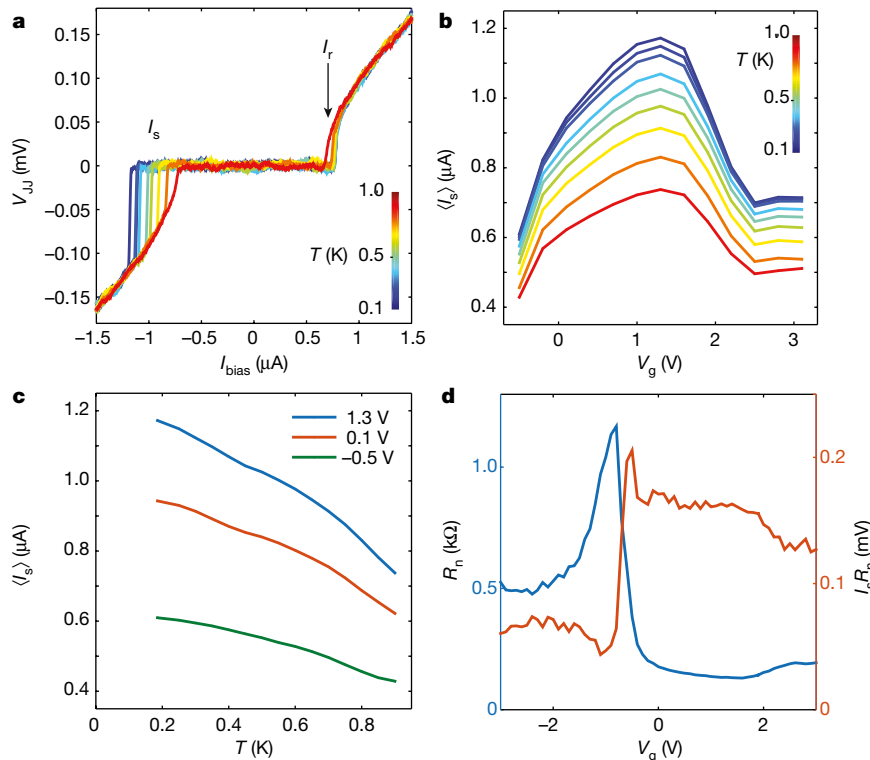


Fig. 2 | Characterization of the GJJ switching current. **a, b,** GJJ voltage as a function of bias current **(a)** and average switching current versus gate voltage **(b)** at temperatures of 0.19–0.9 K. **c,** Average switching current versus

temperature at different gate voltages. **d,** GJJ normal resistance and $\langle I_s \rangle R_n$ as a function of gate voltage.

mediated by supercollision or disorder^{26–29}. However, using the deformation potential of 20 eV and the electron mobility of $20,000 \text{ cm}^2 \text{ V}^{-1} \text{ s}^{-1}$ measured from the GJJ normal resistance versus the gate voltage, the same theory predicts $\Sigma = 0.0086 \text{ W m}^{-2} \text{ K}^{-3}$. We note that Σ ranges from $2.04 \text{ W m}^{-2} \text{ K}^{-3}$ to $9.9 \text{ W m}^{-2} \text{ K}^{-3}$ in the three devices and agrees quantitatively with another report³³. This large discrepancy suggests that the existing electron cooling theories of defect-mediated electron–phonon coupling are not applicable when the mean free path l_{mfp} (340 nm in our sample) is larger than or comparable to the sample dimensions ($0.3 \mu\text{m} \times 2.6 \mu\text{m}$ in our device). A recent scanning nanothermometry experiment³⁴ spatially imaged the cooling of electrons in high-quality graphene and demonstrated that the electron cooling can be dominated by atomic defects on the edge rather than those in the bulk. Therefore, the l_{mfp} value based on the bulk electrical transport may underestimate the total cooling rate of the electron–phonon coupling when l_{mfp} is larger than the sample size. Because such scatterings by atomic defects on the edge scale with the sample perimeter, whereas defect-mediated scattering scales with the sample area, further systematic experiments with consistently etched graphene flakes of different sample aspect ratios can provide greater understanding of the cooling of electrons to achieve a higher-sensitivity graphene-based bolometer in the future.

The effectiveness of the thermal insulation at the graphene–superconductor contacts due to Andreev reflection can be evaluated using the Wiedemann–Franz law. If there is any heat diffusion at the contacts, the GJJ (being wide and short) will have the largest contribution to the thermal conductance, which, based on the one-dimensional thermal model¹⁶, is given by $4(\pi k_B/e)^2(T/R)$ where k_B is the Boltzmann constant, e is the electron charge and R is the electrical resistance between the contacts. For $R_n = 145 \Omega$ at $V_g = 1.9 \text{ V}$, we would expect the thermal conductance through the contacts to be about 387 pW K^{-1} , 1,000 times larger than the actual measured thermal conductance of $G_{\text{th}} = \delta \Sigma A T^{\delta-1} = 230 \text{ fW K}^{-1}$ at 0.19 K. This suggests that the NbN

superconductor used in the experiment acts as a good thermal insulator, prohibiting heat diffusion at the graphene–superconductor interface.

We now study the sensitivity of our detector. When operating as a bolometer, we can infer the input power from the suppression of I_s using the calibration shown in Fig. 4b. The standard deviation of the I_s

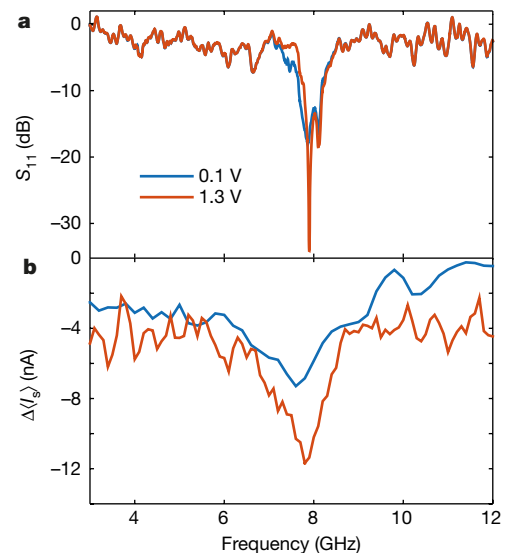


Fig. 3 | Operation of the device as a bolometer and measurement of the detector efficiency. **a,** The scattering parameter S_{11} of the device at 0.19 K shows a resonance near 7.9 GHz with linewidths of 861 MHz and 599 MHz at gate voltages of 0.1 V and 1.3 V, respectively, obtained from the quality factor analysis. **b,** Suppression of the average switching current at -112 dBm relative to the switching current without input power at two different gate voltages.

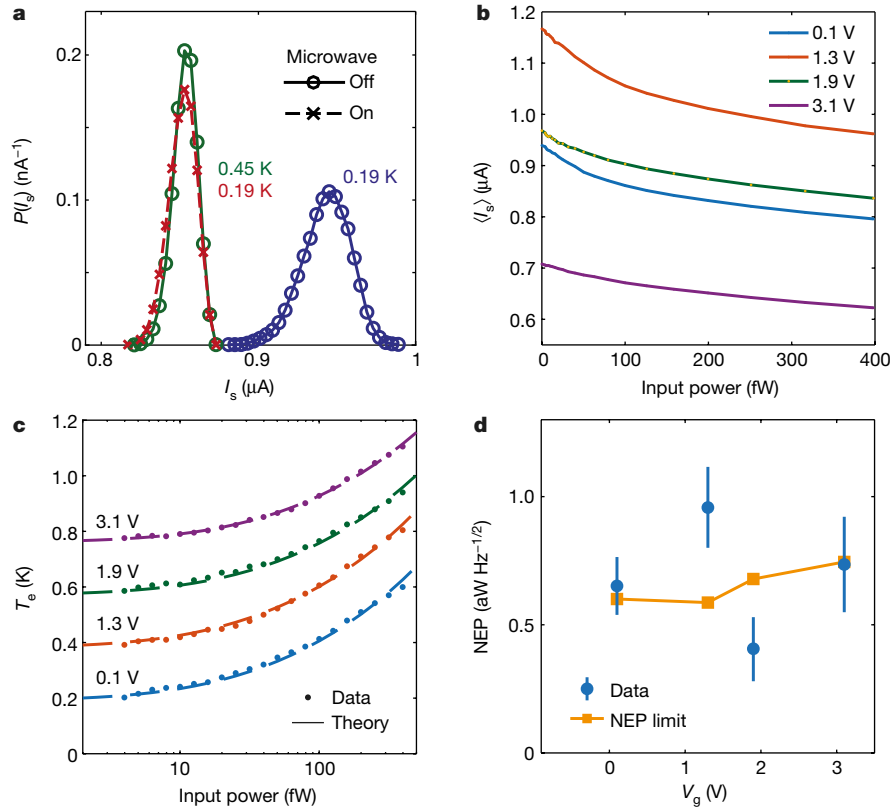


Fig. 4 | Sensitivity and fundamental fluctuation limit of the bolometer.

a, Distributions of the switching current at 0.19 K (blue circles) and 0.45 K (green circles) without microwave input, and at 0.19 K with a microwave input power of 126 fW (red crosses) at $V_g = 0.1$ V. **b**, Average switching current as a function of microwave input power at 7.9 GHz at various gate voltages. **c**, Interpolated graphene electron temperature obtained using the results

shown in Fig. 2c, with 0.19-K offsets for clarity. The dashed lines are fits using the theory of electron–phonon heat transfer. **d**, Measured NEP (blue) and the fluctuation limit (orange). The average NEP is 0.7 ± 0.2 aW Hz $^{-1/2}$, corresponding to an energy resolution of a single 32-GHz photon. The blue error bars are calculated from the fitting errors of $d\langle I_s \rangle/dP_{mw}$ and Δf_{int} with 95% confidence interval.

distribution, σ_{I_s} , sets the uncertainty of a single I_s measurement and thus the minimal detectable power $\delta P_{min} = \sigma_{I_s} (|d\langle I_s \rangle/dP_{mw}|_{P_{mw}=0})^{-1}$; that is, $\delta P_{min} = 11.4$ fW for $\sigma_{I_s} = 13.2$ nA at 0.19 K and $V_g = 1.9$ V. To estimate the noise-equivalent power (NEP), we consider the time required to detect this δP_{min} by comparing three timescales: the resonator input coupling rate, the resonator dissipation rate and the thermal time constant, τ_{th} . Analysis of the scattering parameter of the resonator gives coupling and internal quality factors of 12.8 and 10.0, respectively (see Methods). The resonator is nearly critically coupled with a coupling rate of 630 MHz and a dissipation rate of $\Delta f_{int} = 790$ MHz. The thermal time constant is given by the ratio of the graphene electron heat capacitance C_e to G_{th} . Because $C_e = A\gamma T$ (ref. ²⁵)—where $\gamma = 4\pi^{5/2} k_B^2 n^{1/2} / (3h\nu_F)$ is the Sommerfeld coefficient, n is the electron density, h is Planck's constant and ν_F is the Fermi velocity of electrons in graphene—at 0.19 K and $n \approx 2 \times 10^{12}$ cm $^{-2}$, we obtain $C_e \approx 10 k_B$, resulting in $\tau_{th} \approx 0.6$ ns. Therefore, the shortest GJJ detection time is bounded by the rate at which the resonator dissipates energy into the graphene, so our GJJ bolometer has $NEP = \delta P_{min} / \sqrt{\Delta f_{int}}$. The result is plotted in Fig. 4d and the error is dominated by the accuracy in obtaining $d\langle I_s \rangle/dP_{mw}$ and Δf_{int} . The NEP achieved by this SGS bolometer is 0.7 ± 0.2 aW Hz $^{-1/2}$ (on average across different V_g values).

Compared to the state of the art, our GJJ shows promise for a range of applications. The GJJ bolometer can operate $\sim 10^5$ times faster than the nanowire bolometer owing to its shorter τ_{th} , making the former an attractive component for hot-electron bolometric mixers with ultrawide intermediate-frequency bandwidth. It also has a much lower energy resolution, equivalent to the energy of a single 32-GHz photon¹⁴, because of its small C_e (refs. ^{15,16,18,19}). Unlike the

superconducting-qubit-based and nanowire single-photon detectors, the GJJ detector does not require qubit state preparation, nor does it rely on the breaking of Cooper pairs to generate a detectable signal, so it is suitable for continuous photon sensing over a wide photon energy range.

Intrinsic thermal fluctuation of a canonical ensemble imposes a fundamental limit on the sensitivity of a bolometer, given by $\sqrt{4G_{th}k_B T^2}$ (ref. ¹⁴). Comparison of the data in Fig. 4d suggests that the NEP of our bolometer as predicted by such a fluctuation (using the measurement of the electron–phonon coupling) is in close agreement to the NEP that we measure using the suppression of the switching current that results from the microwave input power. This also suggests that $1/\tau_{th}$ is nearly the same as the internal dissipation rate of the resonator. The same temperature scaling law projects a further improvement to 10^{-21} W Hz $^{-1/2}$ at 20 mK. The same detector design could be used to perform calorimetry to detect single microwave photons with further optimization of $d\langle I_s \rangle/dT$ (ref. ²³). To achieve continuous power readout while keeping the GJJ non-dissipative in the supercurrent state, we can employ a radiofrequency resonance readout to detect the change of the Josephson inductance of the GJJ.

Online content

Any methods, additional references, Nature Research reporting summaries, source data, extended data, supplementary information, acknowledgements, peer review information; details of author contributions and competing interests; and statements of data and code availability are available at <https://doi.org/10.1038/s41586-020-2752-4>.

1. Benford, D., Amato, M., Mather, J. C., Moseley, S. H. & Leisawitz, D. Mission concept for the Single Aperture Far-Infrared (SAFIR) Observatory. *Astrophys. Space Sci.* **294**, 177–212 (2004).
2. Graham, P. W., Irastorza, I. G., Lamoreaux, S. K., Lindner, A. & van Bibber, K. A. Experimental searches for the axion and axion-like particles. *Annu. Rev. Nucl. Part. Sci.* **65**, 485–514 (2015).
3. Govia, L. C. G. et al. High-fidelity qubit measurement with a microwave-photon counter. *Phys. Rev. A* **90**, 062307 (2014).
4. Inomata, K. et al. Single microwave-photon detector using an artificial Λ -type three-level system. *Nat. Commun.* **7**, 12303 (2016).
5. Wei, J. et al. Ultrasensitive hot-electron nanobolometers for terahertz astrophysics. *Nat. Nanotechnol.* **3**, 496–500 (2008).
6. Gasparinetti, S. et al. Fast electron thermometry for ultrasensitive calorimetric detection. *Phys. Rev. Appl.* **3**, 014007 (2015).
7. Govenius, J., Lake, R. E., Tan, K. Y. & Möttönen, M. Detection of zeptojoule microwave pulses using electrothermal feedback in proximity-induced Josephson junctions. *Phys. Rev. Lett.* **117**, 030802 (2016).
8. Lee, G.-H., Jeong, D., Choi, J.-H., Doh, Y.-J. & Lee, H.-J. Electrically tunable macroscopic quantum tunneling in a graphene-based Josephson junction. *Phys. Rev. Lett.* **107**, 146605 (2011).
9. Coskun, U. C. et al. Distribution of supercurrent switching in graphene under the proximity effect. *Phys. Rev. Lett.* **108**, 097003 (2012).
10. Borzenets, I., Coskun, U. C., Jones, S. J. & Finkelstein, G. Phonon bottleneck in graphene-based Josephson junctions at millikelvin temperatures. *Phys. Rev. Lett.* **111**, 027001 (2013).
11. Calado, V. E. et al. Ballistic Josephson junctions in edge-contacted graphene. *Nat. Nanotechnol.* **10**, 761–764 (2015).
12. Ben Shalom, M. et al. Quantum oscillations of the critical current and high-field superconducting proximity in ballistic graphene. *Nat. Phys.* **12**, 318–322 (2016).
13. Wang, J. I.-J. et al. Coherent control of a hybrid superconducting circuit made with graphene-based van der Waals heterostructures. *Nat. Nanotechnol.* **14**, 120–125 (2019).
14. Moseley, S. H., Mather, J. C. & McCammon, D. Thermal detectors as X-ray spectrometers. *J. Appl. Phys.* **56**, 1257–1262 (1984).
15. Vora, H., Kumaravadivel, P., Nielsen, B. & Du, X. Bolometric response in graphene based superconducting tunnel junctions. *Appl. Phys. Lett.* **100**, 153507 (2012).
16. Fong, K. C. & Schwab, K. Ultrasensitive and wide-bandwidth thermal measurements of graphene at low temperatures. *Phys. Rev. X* **2**, 031006 (2012).
17. Yan, J. et al. Dual-gated bilayer graphene hot-electron bolometer. *Nat. Nanotechnol.* **7**, 472–478 (2012).
18. McKitterick, C., Prober, D. & Karasik, B. Performance of graphene thermal photon detectors. *J. Appl. Phys.* **113**, 044512 (2013).
19. Efetov, D. K. et al. Fast thermal relaxation in cavity-coupled graphene bolometers with a Johnson noise read-out. *Nat. Nanotechnol.* **13**, 797–801 (2018).
20. Han, Q. et al. Highly sensitive hot electron bolometer based on disordered graphene. *Sci. Rep.* **3**, 3533 (2013).
21. Cai, X. et al. Sensitive room-temperature terahertz detection via the photothermoelectric effect in graphene. *Nat. Nanotechnol.* **9**, 814–819 (2014).
22. El Fatimy, A. E. et al. Epitaxial graphene quantum dots for high-performance terahertz bolometers. *Nat. Nanotechnol.* **11**, 335–338 (2016).
23. Walsh, E. D. et al. Graphene-based Josephson-junction single-photon detector. *Phys. Rev. Appl.* **8**, 024022 (2017).
24. Tielrooij, K. J. et al. Photoexcitation cascade and multiple hot-carrier generation in graphene. *Nat. Phys.* **9**, 248–252 (2013).
25. Viljas, J. K. & Heikkilä, T. T. Electron–phonon heat transfer in monolayer and bilayer graphene. *Phys. Rev. B* **81**, 245404 (2010).
26. Song, J. C. W., Reizer, M. Y. & Levitov, L. S. Disorder-assisted electron–phonon scattering and cooling pathways in graphene. *Phys. Rev. Lett.* **109**, 106602 (2012).
27. Chen, W. & Clerk, A. Electron-phonon mediated heat flow in disordered graphene. *Phys. Rev. B* **86**, 125443 (2012).
28. Betz, A. C. et al. Supercollision cooling in undoped graphene. *Nat. Phys.* **9**, 109–112 (2013).
29. Graham, M. W., Shi, S.-F., Ralph, D. C., Park, J. & Moeuen, P. L. Photocurrent measurements of supercollision cooling in graphene. *Nat. Phys.* **9**, 103–108 (2013).
30. Tirelli, S. et al. Manipulation and generation of supercurrent in out-of-equilibrium Josephson tunnel nanojunctions. *Phys. Rev. Lett.* **101**, 077004 (2008).
31. Morpurgo, A. F., Klapwijk, T. M. & van Wees, B. J. Hot electron tunable supercurrent. *Appl. Phys. Lett.* **72**, 966–968 (1998).
32. Oelsner, G. et al. Detection of weak microwave fields with an underdamped Josephson junction. *Phys. Rev. Appl.* **7**, 014012 (2017).
33. Draelos, A. W. et al. Supercurrent flow in multiterminal graphene Josephson junctions. *Nano Lett.* **19**, 1039–1043 (2019).
34. Halbertal, D. et al. Imaging resonant dissipation from individual atomic defects in graphene. *Science* **358**, 1303–1306 (2017).

Publisher's note Springer Nature remains neutral with regard to jurisdictional claims in published maps and institutional affiliations.

© The Author(s), under exclusive licence to Springer Nature Limited 2020

Methods

Device fabrication

The devices are fabricated by first encapsulating the monolayer graphene between two layers of atomically flat and insulating boron nitride (~30 nm thick) using the dry-transfer technique. For Device A, the superconducting terminals consist of 5-nm-thick niobium and 60-nm-thick niobium nitride, deposited after reactive ion etching and electron-beam deposition of 5-nm-thick titanium to form the one-dimensional contact^{11,23}. For devices H and T, a molybdenum–rhenium alloy is sputtered as the superconducting material. Finally, we make the local gate to control the carrier density of the monolayer graphene by growing an aluminium oxide dielectric layer by atomic layer deposition before depositing a layer of gold as the metallic gate. All d.c. electrodes are connected through the reactive low-pass filters fabricated on the chip to provide isolation to the microwave circuit. We note that the simultaneous operation of the Josephson junction and the microwave impedance matching of the device can limit the fabrication yield to about 14% when duplicating the process on different sets of cleanroom equipment.

Impact of contact resistance on detector performance

We consider how the contact resistance may affect the device (1) in the Josephson junction measurement and (2) in the microwave resonator. Nyquist noise from the graphene/NbN contact in the junction direction (vertical direction in Fig. 1b–d) is expected to be absent, because the bolometer operates in the supercurrent regime, where the two-probe resistance is zero. Nyquist noise would come into play only after the Josephson junction switches to the resistive regime by microwave photon absorption and gives finite normal resistance R_n . Therefore, we do not need to consider Nyquist noise to determine the NEP of the bolometer. The noise contributions from thermal and quantum fluctuations on the current-biased Josephson junction are included in the determination of the NEP because they both contribute to the width of the switching current distribution in Fig. 4a. These noises induce thermal activation and macroscopic quantum tunnelling of the phase particle of the current-biased Josephson junction³⁵ and their rate can be determined using the Fulton–Dunkleberger method³⁶.

However, it is possible that the contact resistance between the graphene flake and the microwave resonator degrade the bolometer by dissipating the photon energy at the contact instead of at the graphene flake. To estimate this effect, we consider a graphene resistance along the resonator direction of $R_{n,res}$ and a graphene–NbN contact resistance along the resonator (horizontal direction in Fig. 1b–d) of R_c . We measured a normal resistance of $R_n \approx 145 \Omega$ along the direction of a junction with width $W = 1 \mu\text{m}$ and length $L = 270 \text{ nm}$, so the square resistance is $R_{sq} = R_n/(L/W)$. With a graphene width of $W' = 300 \text{ nm}$ and length of $L' = 2.6 \mu\text{m}$ along the resonator direction, we can roughly estimate $R_{n,res} = R_{sq}(L'/W') \approx 5 \text{ k}\Omega$. If we assume that the contact transparencies for graphene–NbN interfaces along the directions of the junction and the resonator are similar, because NbN was deposited at the same time for both the GJJ and the resonator, R_c can be estimated by $R_c = [\pi/(k_F W')] [h/(4e^2)]/\eta \approx 0.4 \text{ k}\Omega$, where k_F is the Fermi wavenumber and $\eta = 0.8$ is the contact transparency estimated from the relationship $R_n = [\pi/(k_F W)] [h/(4e^2)]/\eta$ for ballistic graphene channel along the direction of the Josephson junction (see the next section for a discussion on the ballistic nature of graphene in our experiment). The contact contribution to the photon energy dissipation by R_c is less than 10% of the total resistance, given by $R_{n,res} + R_c$. Thus, we expect that the contact resistance would not considerably degrade bolometer performance.

Electron mean free path

The GJJ is at or near the ballistic limit. This is because if we assume that the graphene is in the diffusive regime, the Drude mobility and mean free path of graphene are estimated to be $20,000 \text{ cm}^2 \text{ V}^{-1} \text{ s}^{-1}$ and 340 nm ,

respectively. However, this mean free path exceeds the junction length of 270 nm . This is usually the case when graphene is encapsulated by atomically flat and insulating hBN flakes and protected from dirty environments during the fabrication process. Ref. ³⁷ describes how the formation of a moiré superlattice with the hBN substrate can give rise to the unusual rise of R_n at $V_g \approx 2\text{--}3 \text{ V}$.

Design of input resonator

We design the device for optimal impedance matching to a $2\text{-k}\Omega$ graphene resistance, a value estimated based on its dimensions. Energy dissipation is dominated by Joule heating into the graphene in such a structure, because the typical internal quality (Q) factor of NbN superconducting resonators without a graphene flake is of the order of $10^5\text{--}10^6$, whereas the internal Q factor of our device is measured to be less than 30, using the circle fitting method³⁸ and fitting of the loaded Q factor (see Extended Data Fig. 1). We achieve optimal impedance matching at the critical coupling (where the internal Q factor of the resonator due to the graphene resistance is equal to the Q factor of the coupling) by adjusting the coupling gap capacitor. We simulate the device with different gap capacitor values using a method-of-moments electromagnetic simulator and determine a coupling capacitor value of 200 fF . In addition to reflectometry (Fig. 3a), we can also measure the input resonator frequency by monitoring I_s , as shown in Extended Data Fig. 2.

Electron–phonon coupling

We can use the electron–phonon coupling theory in the supercollision or disorder regime to calculate Σ (refs. ^{26,27}):

$$\Sigma = \frac{2\zeta(3)}{\pi^2} \frac{E_F}{v_F \rho_M} \frac{\mathcal{D}^2 k_B^3}{\hbar^4 l_{\text{mfp}} s^2}, \quad (1)$$

where ζ is the zeta function, E_F is the Fermi energy of the graphene charge carriers, ρ_M is the mass density of the graphene sheet, \mathcal{D} is the deformation potential, \hbar is the reduced Planck constant and s is the sound velocity of the graphene lattice. However, the enhanced electron–phonon cooling that we observed is more probably due to resonant scattering by defects located around the edges of the graphene flake^{33,34,39}. The fitted Σ values listed in Extended Data Table 1 are based on the data in Extended Data Figs. 3, 4.

Σ is independent of the charge carrier density, assuming that the electron mobility μ_e is also independent of the carrier density such that $\mu_e = e\tau/m = ev_F l_{\text{mfp}}/E_F$, where τ and m are the scattering time and mass of the charge carriers, respectively. The measured electrical transport and Josephson junction parameters are listed in Extended Data Table 2.

Data availability

The data that support the findings of this study are available from the corresponding author upon reasonable request.

35. Martinis, J. M., Devoret, M. H. & Clarke, J. Experimental tests for the quantum behavior of a macroscopic degree of freedom: the phase difference across a Josephson junction. *Phys. Rev. B* **35**, 4682–4698 (1987).
36. Fulton, T. A. & Dunkelberger, L. N. Lifetime of zero-voltage state in Josephson tunnel junctions. *Phys. Rev. B* **9**, 4760–4768 (1974).
37. Ponomarenko, L. A. et al. Cloning of Dirac fermions in graphene superlattices. *Nature* **497**, 594–597 (2013).
38. Khalil, M. S., Stoutimore, M. J. A., Wellstood, F. C. & Osborn, K. D. An analysis method for asymmetric resonator transmission applied to superconducting devices. *J. Appl. Phys.* **111**, 054510 (2012).
39. Kong, J. F., Levitov, L., Halbertal, D. & Zeldov, E. Resonant electron-lattice cooling in graphene. *Phys. Rev. B* **97**, 245416 (2018).

Acknowledgements We acknowledge discussions with L. Levitov, M.-H. Nguyen and W. Kalfus. We thank H.-J. Lee for fabrication facility support for some of the devices. W.J. and G.-H.L. acknowledge support from the Samsung Science and Technology Foundation under Project Number SSTFBA1702-05. D.K.E. acknowledges support from the Ministry of

Article

Economy and Competitiveness of Spain through the “Severo Ochoa” programme for Centres of Excellence in R&D (SE5-0522), Fundació Privada Cellex, Fundació Privada Mir-Puig, Generalitat de Catalunya through the CERCA programme, the H2020 Programme under grant agreement 820378 (project 2D-SIPC) and the La Caixa Foundation. The work of E.D.W. and D.E. was supported in part by the Army Research Laboratory Institute for Soldier Nanotechnologies programme W911NF-18-2-0048 and the US Army Research Laboratory (award W911NF-17-1-0435). K.W. and T.T. acknowledge support from the Elemental Strategy Initiative conducted by MEXT, Japan, grant number JPMXP0112101001, JSPS KAKENHI grant number JP20H00354 and CREST(JPMJCR15F3), JST. The work of P.K. and K.C.F. was supported by the US Army Research Office under Cooperative Agreement number W911NF-17-1-0574.

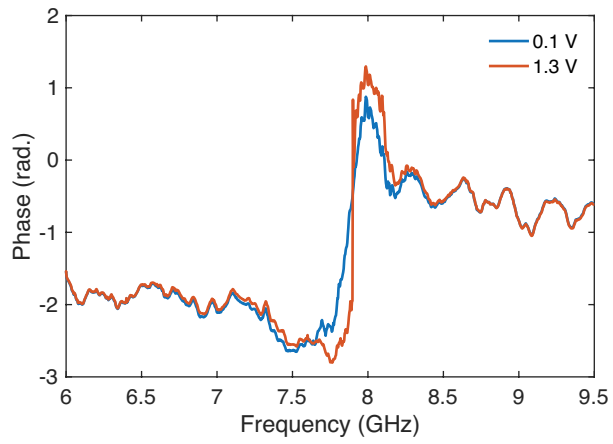
Author contributions G.-H.L., T.A.O., D.E. and K.C.F. conceived the project. L.R., G.-H.L. and W.J. designed and fabricated the samples. T.T. and K.W. provided the hBN crystal. G.-H.L., E.D.W. and K.C.F. performed the measurements. G.-H.L., D.K.E., L.R., E.D.W., T.A.O., P.K., D.E. and K.C.F. performed the data analysis and wrote the paper. P.K., D.E. and K.C.F. supervised the project.

Competing interests The authors declare no competing interests.

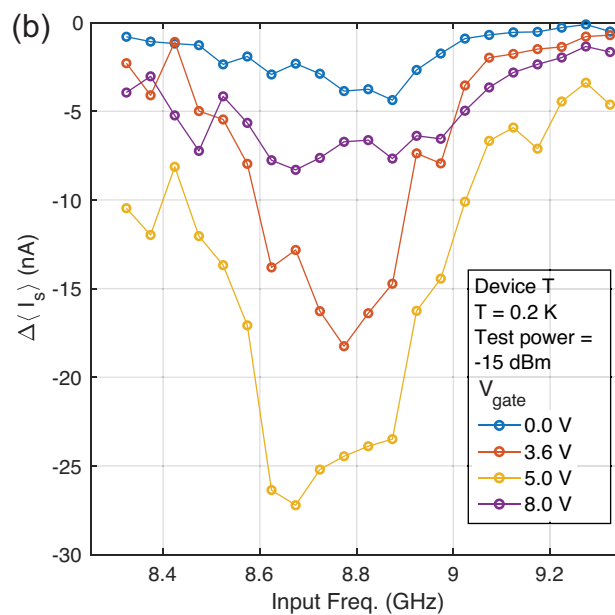
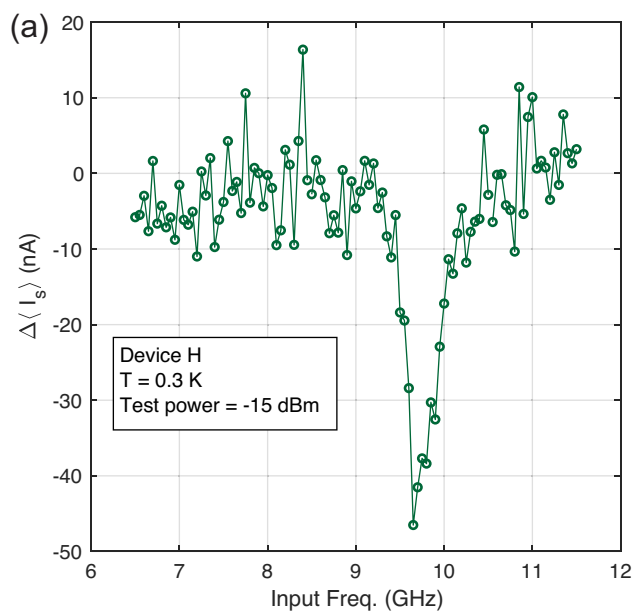
Additional information

Correspondence and requests for materials should be addressed to K.C.F.

Reprints and permissions information is available at <http://www.nature.com/reprints>.

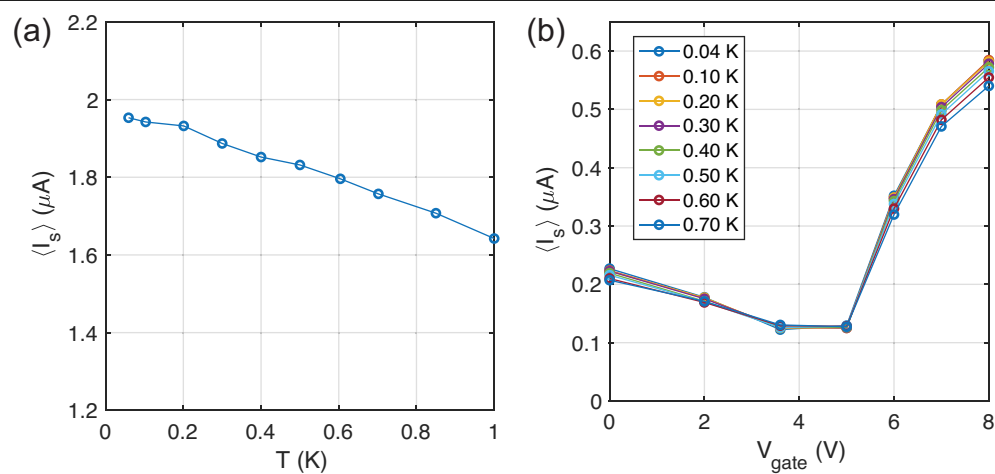


Extended Data Fig. 1 | Loaded Q factor of input resonator. Fitting of the loaded quality factor of the microwave resonator. Shown is the phase of the S_{11} scattering parameter of the half-wave microwave resonator at two different gate voltages. Data from the same dataset as in Fig. 3a.

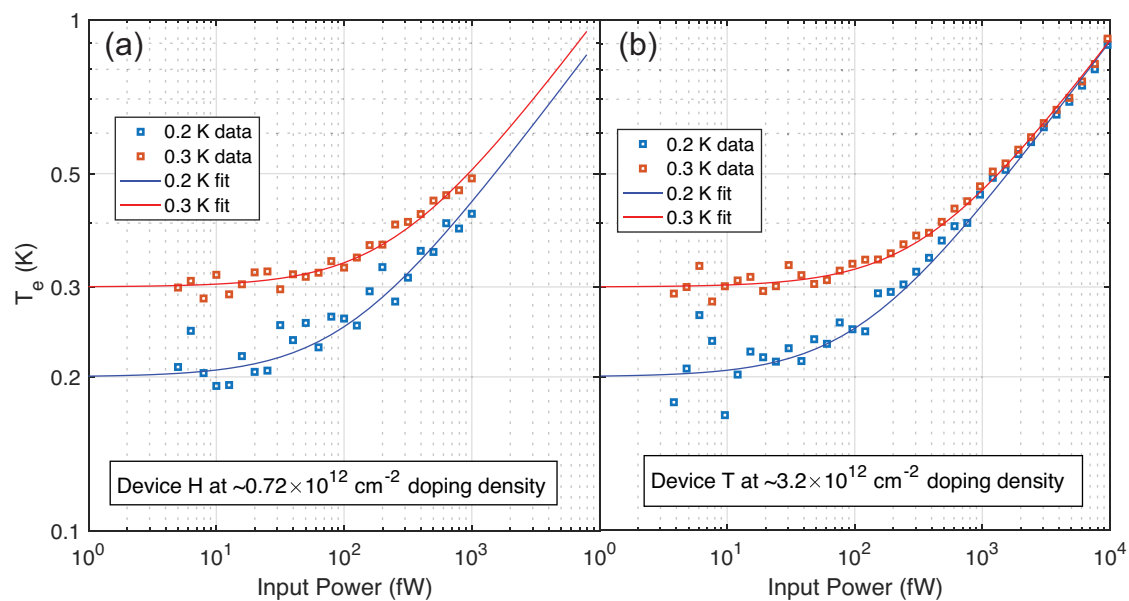


Extended Data Fig. 2 | GJJ bolometer input resonator. a, b, Suppression of the switching current at the resonance frequency of the input resonator for Device H (a) and Device T (b) with test power of -15 dBm applied outside the

cryostat at 0.3 K (a) and 0.2 K (b). See Extended Data Table 1 for the dimensions and measured parameters of the devices.



Extended Data Fig. 3 | GJJ switching current. a, b, Average switching current of the Josephson junction for Device H (a) and Device T (b).



Extended Data Fig. 4 | Electron cooling. **a, b,** Interpolated graphene electron temperature versus input power for Device H with a carrier density of $\sim 0.72 \times 10^{12} \text{ cm}^{-2}$ (**a**) and Device T with a carrier density of $\sim 3.2 \times 10^{12} \text{ cm}^{-2}$ (**b**). The lines are fits using the electron-phonon heat transfer theory.

Extended Data Table 1 | Sensitivity and thermal properties of the GJJ bolometer

	Device A				Device H			Device T		
superconductor	NbN				MoRe			MoRe		
graphene area (μm^2)	0.78				1.00			1.40		
input frequency (GHz)	7.9				9.75			8.82		
temperature (K)	0.2				0.2	0.3	0.5	0.2		
V_{gate} (V)	0.1	1.3	1.9	3.1	~ 1			6	7	8
V_{CNP} (V)	-0.9				~ -1			3.6		
carrier density (10^{12} cm^{-2})	0.72	1.6	2.0	2.9	~ 0.72			1.7	2.5	3.2
R_{n} (Ω)	160	127	145	195	150			249	225	205
C_e (k_{B})	6.1	9.0	10	12	6.1	9.7	16	10	12	14
Σ ($\text{Wm}^{-2}\text{K}^{-3}$) from fitting	2.1	2.0	2.7	3.3	15	9.9	6.3	6.8	9.5	9.6
G_{th} (pW/K)	0.181	0.173	0.231	0.279	1.80	2.68	4.75	1.1	1.9	1.6
$\langle I_{\text{s}} \rangle$ (μA)	0.943	1.17	0.978	0.714	1.932	1.887	1.832	0.349	0.508	0.582
$\sigma_{I_{\text{s}}}$ (nA)	15.0	23.7	13.2	9.96	25.8	26.2	21.4	3.35	4.21	4.48
$ d\langle I_{\text{s}} \rangle/dP $ (10^6 A/W)	1.1	1.5	1.2	0.43	0.18	0.11	0.081	0.014	0.022	0.018
Q_{int}	18.3	28.5	10.0	7.9	~ 39			190	228	242
Q_{couple}	18.4	24.4	12.8	9.7	~ 39			25	25	26
resonator internal dissipation rate (MHz)	432	277	790	1000	~ 250			46	39	36
thermal fluctuation limited NEP ($\times 10^{-19} \text{ W/Hz}^{-1/2}$)	0.60	0.59	0.68	0.75	2.0	3.6	8.1	1.59	1.87	1.84
estimated NEP ($\times 10^{-19} \text{ W/Hz}^{-1/2}$)	6.5	9.6	4.1	7.4	8.9	15	17	35	28	40
ratio of the estimated NEP to the thermal fluctuation limited NEP	1.1	1.6	0.6	1.0	4.9	4.2	2.0	22	15	22

Parameters used to estimate the NEP and thermal properties of the GJJ bolometer. Data presented in the main text are collected from Device A.

Josephson junction parameters of Device A at $V_{\text{gate}} = 1.9 \text{ V}$	
JJ channel length	300 nm
JJ channel width	1 μm
Electron density	$2.0 \times 10^{12} \text{ cm}^{-2}$
Electronic mobility	$2 \times 10^4 \text{ cm}^2/\text{Vs}$
normal resistance	59 Ω
Mean free path	340 nm
Disorder temperature	2.8 K
Bloch-Grüneisen temp.	76 K
$I_c(T_0)R_n$ product	142 μeV
Thouless energy	1.2 meV
JJ coupling energy	2.0 meV
Effective capacitance	3.65 fF
Plasma Freq. at zero bias current	$\leq 904 \text{ GHz}$
McCumber parameters	0.23
NbN superconducting gap	1.52 meV